Interplay between bulk self-assembly, interfacial and foaming properties in a catanionic surfactant mixture of varying composition

José Ferreira, Alesya Mikhailovskaya, Alexis Chenneviere, Frédéric Restagno, Fabrice Cousin, François Muller, Jéril Degrouard, Anniina Salonen, Eduardo F Marques

Interplay between bulk self-assembly, interfacial and foaming properties in a catanionic surfactant mixture of varying composition†

José Ferreira,[ab] Alesya Mikhailovskaya,[b] Alexis Chenneviere,[c] Frédéric Restagno,[b] Fabrice Cousin,[c] François Muller,[c] Jéril Degrouard,[b] Anniina Salonen *[b] and Eduardo F. Marques *[a]

The self-aggregation, surface properties and foamability of the catanionic surfactant mixture cetyltri-methylammonium bromide (CTAB)/sodium octyl sulfonate (SOSo) have been investigated to obtain insight on the relation between bulk nanostructures, surfactant packing, and foam stability and aging. Light microscopy, SANS, cryo-TEM, DLS, surface tension, rheometry and direct photography were used to characterize mixtures with varying CTAB molar fraction, x_{CTAB}. In the bulk, self-assembly is richer in the excess CTAB region than in the excess SOSo one. Starting from neat CTAB micelles and on addition of anionic surfactant, there is a change from small ellipsoidal micelles ($1 < x_{CTAB} \leq 0.80$) to large rodlike micelles ($0.65 \leq x_{CTAB} \leq 0.55$) and then to vesicles ($0 < x_{CTAB} \leq 0.50$), with coexistence regions in between; SOSo-rich mixtures are thus dominated by vesicles. High size polydispersity for the micelles and vesicles is an intrinsic feature of this system. Foam stability is concomitantly impacted by x_{CTAB}. SOSo is a small mobile molecule and so it disrupts foam stability, irrespective of the presence of vesicles. Foams are thus only stable in the CTAB-rich regions, and SANS shows that the shape of micelles and vesicles is unchanged inside the foam. Foam drainage is thereby mostly controlled by the presence of the elongated micelles through the solution viscosity, whereas coarsening is influenced by dense surfactant packing at the gas–liquid interfaces.

1. Introduction

Strongly associative behavior in aqueous surfactant mixtures leads to a diversity of self-assembled structures, whose size and shape is mainly controlled by the surfactant mixing ratio and total concentration.[1–3] The bulk assemblies—micelles, vesicles, nanotubes, liquid crystals and other structures—are important in many applications such as nano-reactor chemistry,[4] solubilization,[5,6] soft templating,[7–9] rheological control[10–12] or molecular transport.[13–15] The interfacial properties of the mixed surfactants also undergo important modifications.[16,17] Surface activity, insoluble monolayer phase behavior, surface rheology and foamability are examples of properties that are often significantly changed from those of the individual surfactants owing to the strong interactions generated. With respect to foams, the extent to which surfactant self-assembly in the bulk of the mixture affects foam stability and aging remains an open question, calling for more experimental investigations and the addressing of systems with assorted molecular properties.[18–25]

Liquid foams are present throughout nature and are widely used in commercial applications and industrial processes.[26] Their unique properties and easy generation are a good working model for the fundamental understanding of soft material properties.[26,27] Considering this variety of applications, it is of critical importance to understand foam stability and aging processes in order to obtain suitable foam lifetimes. To improve foam stability one can act on three main aging mechanisms: drainage, coarsening and coalescence.[26,28–30] Drainage can be slowed down by increasing bulk viscosity[24,31] while controlling the coarsening mechanism involves using low-solubility gases or enhancing the solid-like character of surfactant films at the bubble surface.[19,22,24] Coalescence can be negligible, as long as the bubbles are not too big or the foam too dry, in the presence of good stabilizers that provide steric or electrostatic repulsions between interfaces, or interfacial elasticity.[23,32] The presence of

[a] Centro de Investigação em Química, Department of Chemistry and Biochemistry, Faculty of Science, University of Porto, Rua do Campo Alegre s/n, 4169-007 Porto, Portugal. E-mail: efmarque@fc.up.pt

[b] Laboratoire de Physique des Solides, CNRS UMR8502 and Univ. Paris-Sud, Université Paris-Saclay, 91405 Orsay Cedex, France. E-mail: anniina.salonen@u-psud.fr

[c] Laboratoire Léon Brillouin, CEA Saclay, 91191 Gif sur Yvette Cedex, France

† Electronic supplementary information (ESI) available. See DOI: 10.1039/c7sm01601h

particles, polymers, liquid crystals or emulsion droplets can render the solution viscoelastic also slowing or even arresting drainage.[18,24,25,33–36] Many studies have been carried out to try and elucidate the link between molecular structure and foam stability, where among other effects surfactant chain length,[37–39] headgroup type[40] and degree of dimerization[41] have been systematically explored.

Enhanced surface adsorption and multifaceted self-assembly are key features in mixtures of cationic and anionic surfactants.[42–46] These effects stem mostly from the electrostatic interaction between the headgroup opposite charges that leads to counterion release and large positive entropy.[42–45,47] These versatile properties make catanionic systems especially amenable to investigate the interplay between bulk properties and interfacial stability in foams[18–22] and emulsions.[48,49] There are a few reports available on the foaming behavior,[18–22] but many questions remain still open. Varade *et al.*[18] have shown that the formation of densely packed monolayers, and the entrapment of vesicles inside the Plateau borders and thin films greatly reduce or even stop foam drainage and coarsening. Fauser *et al.*[20] found that foam film properties are strongly affected by the ratio between the oppositely charged surfactants allowing the tuning of foam film stability. Xue *et al.* showed that wormlike micelles can help stabilize CO_2 in water foams by slowing down film drainage.[21] Catanionic mixtures with high asymmetry in surfactant chain lengths and hence solubility—like the CTAB/SOSo under investigation here—are particularly interesting candidates to study, as the variation in mixing ratio leads to the assembly of rodlike or wormlike micelles and vesicles.[42,44,50–54] In a previous work with the salt-free equimolar surfactant (TASo) derived from this mixture, our focus was the bulk assembly and temperature-dependent shape transitions.[55]

In the current work, the main purpose was to investigate the aggregation behavior of the strongly asymmetric catanionic mixture CTAB/SOSo as function of surfactant composition, and how the bulk assemblies and surfactant packing affect foam stability and aging. We first address the aggregated structures in solution varying x_{CTAB} at fixed temperature and surfactant concentration (20 mmol kg^{-1}), and resorting to microscopy (light and cryo-TEM) and SANS as the main probing tools. Surface tension and viscosity characterization follow. We then investigate the aggregates present inside the foams by SANS and characterize foam formation and drainage as a function of x_{CTAB}. As will be shown, x_{CTAB} impacts significantly self-assembly, surface properties, viscosity and the foaming behavior. Ultimately, we aim at establishing the links between the latter properties and increasing our understanding of foaming patterns and mechanisms in highly associative surfactant mixtures.

2. Experimental section

2.1. Sample preparation

The surfactants cetyltrimethylammonium bromide (CTAB) and sodium octyl sulfonate (SOSo) were purchased from Sigma-Aldrich with 99% purity. CTAB was twice recrystallized in diethyl ether and SOSo was used without further purification. Concentrations in this work are expressed in molality (surfactant amount per kg of solvent). The *cmc* values obtained by surface tension, 0.91 and 153 mmol kg^{-1} for CTAB and SOSo, respectively, confirmed good purity. The catanionic mixtures were prepared by weight from stock solutions of each surfactant in Milli-Q® ultrapure water or in D_2O for some of the experiments (as noted *in situ*). The mixtures were subject to gentle mixing for at least 24 hours and then left undisturbed for the same period before any measurements. All mixtures have a total CTAB + SOSo 20.0 mmol kg^{-1} concentration and the mixing ratio is expressed as the molar fraction of CTAB:

$$x_{CTAB} = \frac{n_{CTAB}}{n_{CTAB} + n_{SOSo}} \quad (1)$$

2.2. Video-enhanced light microscopy

A polarized light microscope Olympus BX51, equipped with differential interference contrast (DIC), was used. The images were captured by an Olympus C5060 digital camera. Observation was carried out in sealed slip/slide preparations.

2.3. SANS

SANS experiments were performed in Laboratoire Léon Brillouin, at CEA/Saclay. Incoming polychromatic neutrons are monochromatized by a mechanical velocity selector. The BF_3 multi-detector, with 128 × 128 cells of 5 × 5 mm^2, was positioned at 1 m with λ_n = 6 Å for high q, 3 m with λ_n = 6 Å for medium q, 5 m with λ_n = 8.5 Å for low q and 6.7 m with λ_n = 15 Å for very low q distances from the sample in the horizontal direction in its vacuum tube. Samples were analyzed in 1 mm high quality quartz cells. The 2D isotropic scattering spectra were corrected for detector efficiency by dividing the scattering pattern by the incoherent scattering spectra of neat water, and were radially averaged and converted to absolute scale. Background was subtracted using the constant value of the incoherent scattering measured at high q values. This treatment and all data fittings shown below were performed using the PASiNET v2.0146 software according to standard procedures.[56]

2.4. Cryo-TEM

Aliquots of the samples (3 μL) were deposited onto a glow-discharged holey carbon grid (Quantifoil R2/2). The grid was blotted with a filter paper and directly plunged into liquid ethane cooled down by liquid nitrogen, using a FEI Vitrobot operated at 22 °C and 100% relative humidity. The cryo-specimens were transferred into a Gatan 626 cryo-holder and observed at −180 °C in a JEOL 2010F Transmission Electron Microscope operated at 200 kV. Images were recorded on a Gatan Ultrascan 4K camera with −1.5 to −2.5 μm of defocus at a magnification of 50 000 under low electron-dose conditions.

2.5. Surface tension

Surface tension of the solutions was measured with a Dataphysics DCAT 11 tensiometer (Wilhelmy plate), with the SCAT 11 software.

The experiments were carried out at a temperature 27.0 ± 0.1 °C, controlled by a Julabo thermostated bath.

2.6. Viscosity

The samples were transferred into a Rheoplus (Anton Paar) rheometer after at least 24 h of equilibration. Viscosity was measured with a Couette geometry in a log ramp shear rate from 1 to 100 rad s^{-1}. The cup and bob system had a internal gap thickness of 0.42 mm, external gap thickness of 0.47 mm and a sample volume of 3.619 mL.

2.7. Foam generation and stability

Foams were generated by the double syringe method.[57] This method makes use of two 50 mL syringes from CODAN Medical, and a plastic tube junction with inner diameter of 4.3 mm. The syringes were washed with ultrapure water several times before the foaming process. The surfactant mixture needed for the foaming was extracted and measured from the glass vials directly with a micropipette, whereas the amount of gas was controlled by the syringe indicators. A mixture of air and C_6F_{14} was used in SANS and drainage experiments. Air was passed through liquid C_6F_{14} and incorporated in the syringe where the surfactant solution is already set.

To measure drainage velocity, the different foams were stored in glass vials and photos were taken in controlled intervals of time. The front of the rising liquid at the bottom of the vial was followed in each image and its distance to the vial bottom measured. Knowing the time interval between photos and the liquid height at each one, a linear regression is calculated with the first points, where the slope is proportional to the volumetric rate of drainage. Dividing the measured rate by the liquid fraction, φ, gives an estimate of the drainage velocity, v. To measure bubble size, a foam sample was collected, placed over a lamella and diluted in the same bulk solution from where the foam was generated. Average bubble size is then determined by light microscopy, averaging over at least 500 bubbles.

3. Results and discussion

3.1. Phase behavior and foamability of CTAB/SOSo mixtures: preliminary observations

CTAB/SOSo mixtures at 20.0 mmol kg^{-1} and different x_{CTAB} were subject to ocular and light microscopy observations to get initial information on the phase and foaming behaviors, as shown in Fig. 1. The temperature for all of the studies was set at 27 °C, so as to lie a few degrees above the Krafft temperature of CTAB (≈25 °C). A clear dependence of both behaviors on surfactant mixing ratio was seen, in line with other catanionic systems.[42,50,52,58–60] Cationic-rich samples ($x_{CTAB} > 0.50$) present a consistent bulk transparency, while at equimolarity a bluish dispersion is formed. Anionic-rich mixtures for x_{CTAB} = 0.33 and 0.25 eventually phase-separate by creaming, while for $x_{CTAB} < 0.25$ they appear bluish or hazy. Under the light microscope, the bluish samples with x_{CTAB} = 0.50, 0.20 and 0.10 show vesicles of 0.5–15 μm in diameter alongside clusters of irregular structures (Fig. 1B–D) indicating high polydispersity; no birefringent multilamellar structures are found. Transparent mixtures, on the other hand, show no evidence for these aggregates under the resolution of the light microscope. Foams generated by vigorous shaking (Fig. 1E) also show varying behavior. While cationic-rich and equimolar samples typically foam well (though foam drainage varies widely with composition), anionic ones foam poorly or not at all, and the foam is clearly very unstable. To establish a link between bulk self-assembly and

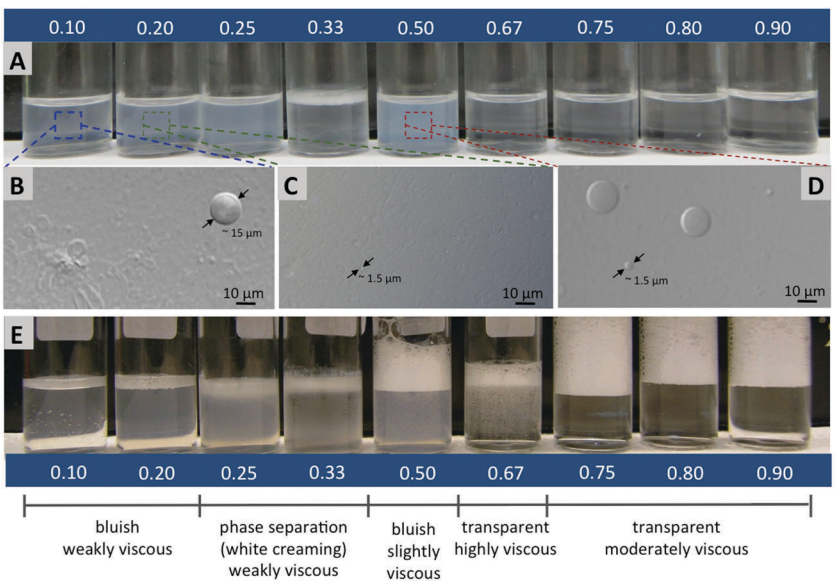

Fig. 1 Observations for 20 mmol kg^{-1} CTAB/SOSo mixtures at 27 °C with varying x_{CTAB}: (A) visual appearance for the full x_{CTAB} range studied; (B–D) 0.10, 0.20 and 0.50 bluish samples, respectively, imaged by light microscopy showing giant μm-sized vesicles (~1–15 μm), as indicated by the arrows; (E) foams generated by vigorous shaking.

foaming properties, we proceeded to detailed characterization studies.

3.2. Bulk self-assembly: from small micelles to polydisperse vesicles

Mixtures with varying x_{CTAB} were characterized by SANS and cryo-TEM (complemented by dynamic light scattering) in order to probe morphology and characteristic sizes, together with viscosity data to obtain the rheological behavior. The preliminary observations described before already gave some indication for polydisperse aggregates and therefore complementary characterization techniques were warranted for an in-depth picture. For simplicity and because some of the most interesting effects were observed in the CTAB-rich side, the results are described on the basis of decreasing x_{CTAB}, that is, in the order of increasing concentration of SOSo in the mixture. SANS is an extremely powerful tool to unravel the structure of soft matter and surfactant mixtures in particular.[51–57] The data in Fig. 2 show three types of aggregate structures derived from the respective scattering patterns. The characteristic sizes obtained by the fitting process

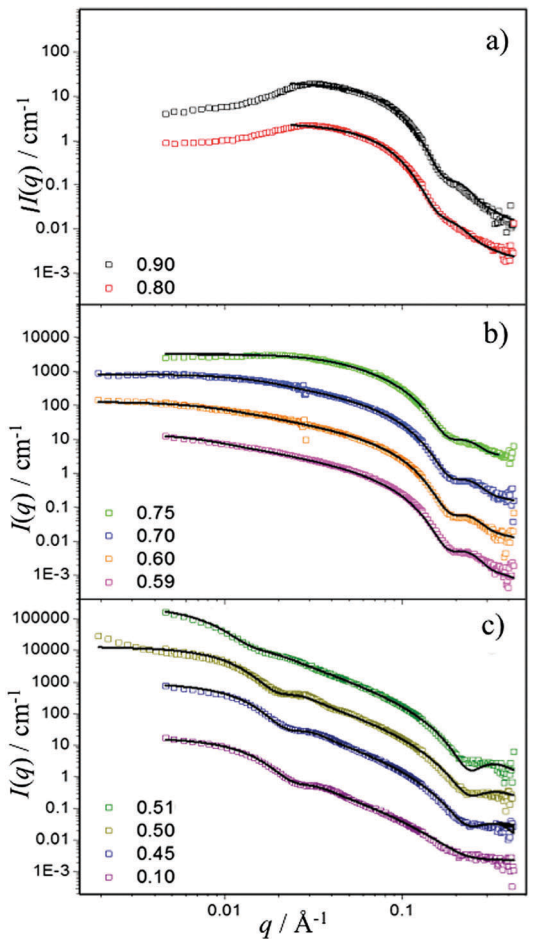

Fig. 2 SANS spectra and respective fittings of bulk mixtures at varying x_{CTAB}: (a) 0.80 and 0.90, (b) 0.59, 0.60, 0.70, 0.75, and (c) 0.10, 0.45, 0.50, 0.51. For easier tracking, the scattering intensity of samples 0.90, 0.60 and 0.45 were multiplied by a factor of 10, samples 0.70 and 0.50 by 100 and samples 0.75 and 0.51 by 1000.

Table 1 Characteristic sizes and form factors obtained by SANS

x_{CTAB}	Radius a/nm	Radius b/nm	Form factor
0.90	2.0 ± 0.1	3.2 ± 0.1	Ellipsoids
0.80	2.0 ± 0.1	3.4 ± 0.1	
	Length/nm	Radius/nm	
0.75	9.2 ± 0.1	2.1 ± 0.1	Rods
0.70	27.0 ± 0.2	2.0 ± 0.1	
0.60	40.5 ± 0.9	2.0 ± 0.1	
0.59	44.2 ± 0.8	2.0 ± 0.1	
	Radius/nm	Thickness/nm	
0.51	12.6 ± 0.2	2.6 ± 0.1	Vesicles
0.50	11.6 ± 0.1	2.6 ± 0.1	
0.45	10.4 ± 0.1	2.6 ± 0.1	
0.10	9.0 ± 0.1	2.2 ± 0.1	

are presented in Table 1. For samples 0.90 to 0.80, Fig. 2a, a good fit is obtained using an ellipsoidal particle form factor. The ellipsoids in sample 0.80 are slightly more elongated than those for 0.90 while having similar radii, but the shapes are very similar to neat CTAB micelles.[58] Between samples 0.75 and 0.59, Fig. 2b, the data can be fitted with a form-factor of rodlike structures. A form factor for worms was also tested but it was ruled out, as the persistent length calculated was higher than the worm length, indicating that the shape is in fact closer to a rigid rod. From the fitted data, there is an increase in rod length from 9 to 44 nm (together with a small increase in polydispersity) as x_{CTAB} decreases, while the cross section radius stays constant at $\approx$2 nm. From samples 0.51 to 0.10, Fig. 2c, the scattering profiles are consistent with vesicles (Table 1), in qualitative agreement with sample turbidity and the microscopy observations. The SANS average radius of the vesicles is, however, very small, decreasing from 13 to 9 nm as x_{CTAB} decreases. As x_{CTAB} changes the packing in the bilayers changes, and the bilayer thickness is around 2.6 nm in the range 0.51–0.45 and slightly thinner (2.2 nm) for 0.10.

To obtain further data on the elongated micelles and vesicles prepared in H_2O, samples 0.60, 0.53 and 0.50 were imaged by cryo-TEM (Fig. 3). For 0.60, elongated threadlike micelles with fairly long apparent persistence lengths are seen, with contour lengths between 20 and few hundred nm (Fig. 3A), as measured from SANS. In contrast, sample 0.53 evidence the coexistence of vesicles (r = 6 to 80 nm) and elongated micelles ranging from 10 to several hundred nm long (Fig. 3B). Finally, at 0.50 (equimolarity) only polydisperse vesicles with radii ranging from 10 to 300 nm are found (Fig. 3C). No evidence for large vesicles was found from the SANS measurements, possibly because in cryo-TEM one searches for areas where objects are present, hence concentrating on larger objects, although their real concentration may be low. The slight upturn at very low q for x_{CTAB} = 0.50, Fig. 2c, could be indeed an indication of a few large vesicles.

DLS measurements provided further data to complete qualitatively the picture (see Fig. S1, ESI†). The intensity size distribution for x_{CTAB} = 0.90–0.75 show broad peaks around 4 nm consistent with small micelles, together with a shallow

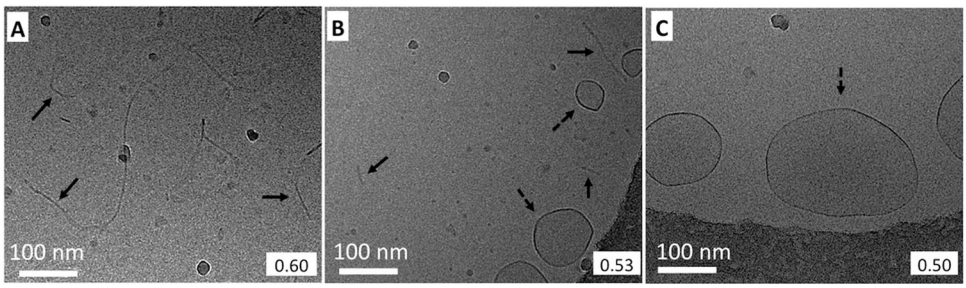

Fig. 3 Cryo-TEM imaging of samples with x_{CTAB} equal to (A) 0.60 (B) 0.53 and (C) 0.50; the full and dashed arrows point to elongated micelles and vesicles, respectively.

peak at higher sizes (100–1000 nm) that could signal already the presence of large micelles (no vesicles were detected by microscopy). At 0.67 a broad peak centered at ≈20 nm is in line with the elongated micelles captured by SANS and cryo-TEM. Samples with $x_{CTAB} \geq 0.50$ show highly polydisperse aggregates from 50 nm to more than 1000 nm, in agreement with the vesicles observed by light and electron microscopies, but larger than found by SANS. Zeta potential, ζ, measurements for $x_{CTAB} < 0.50$ do not yield meaningful data (presumably due to polydispersity), but the 0.50 sample gives $\zeta \approx +38$ mV. This positive and relatively high zeta potential is very interesting, indicating that despite equimolar composition, the vesicles do not have zero charge likely due to the higher unimer solubility of SOSo (another hypothesis is that SOSo resides preferentially in the inner monolayer of the vesicle). The anionic-rich samples 0.20 and 0.10 yielded $\zeta \approx -10$ mV and -20 mV, respectively, in line with the high content in anionic surfactant. The previous results indicate that different types of self-assembled structures are formed as the surfactant mixing ratio varies. To investigate the effect of microstructure on rheological behavior, the viscosity as a function of x_{CTAB}, at fixed shear rate, was probed in the region 0.90–0.40 for samples prepared in H_2O, as shown in Fig. 4. Viscosity was also measured as a function of the shear rate (see Fig. S2, ESI†).

The viscosity remains very low between 0.90–0.70, where ellipsoidal micelles are dominant. However, it increases dramatically when x_{CTAB} goes from 0.70 to 0.60 (by a 40-fold factor), in line with the presence of stiff elongated micelles and long range interactions. Moreover, the sample at 0.60, where viscosity peaked, also shows a shear-thinning behavior (Fig. S2, ESI†). It is likely that transient entanglements[61,62] between the elongated micelles lie behind this very high viscosity; breakage of these physical bonds and alignment effects[63] take place when the shear rate increases. Viscosity then drops in the range 0.60–0.52, where vesicles form at the expense of the large micelles. For roughly $x_{CTAB} \geq 0.50$ where only vesicles are present, the viscosity goes down to the base level of *ca.* 2 mPa s^{-1} (slightly above the value of neat water, at 25 °C).

In summary, we have shown that starting from neat CTAB there is a shape change and increase in size of the aggregates. Small ellipsoidal micelles dominate initially ($x_{CTAB} < 0.75$), but they are gradually replaced with long rodlike micelles that dominate in the region of 0.65–0.55; for $x_{CTAB} \geq 0.50$ the behavior is dominated by polydisperse vesicles. The viscosity of the solutions is dramatically increased in presence of the elongated micelles.

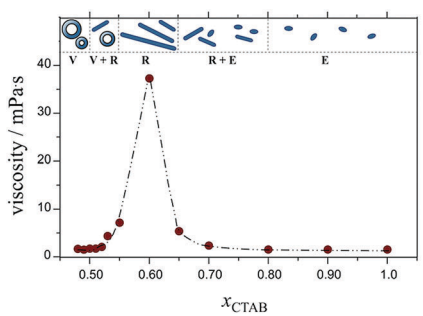

Fig. 4 Viscosity as a function of the x_{CTAB} for a fixed shear rate of 7.20 s^{-1}, at 27 °C (line is a visual guide). At the top, a schematic view of the aggregates present as x_{CTAB} varies, with the approximate location of the boundaries between aggregation states; E, ellipsoidal micelles; R, long rodlike micelles, V, vesicles.

3.3. Strong synergism from surface tension data

It was clear from the previous studies that the two surfactants interact strongly in solution to yield aggregates of varying shape and size. To further analyze the magnitude of this interaction and the consequent non-ideal effects, surface tension curves—γ *vs.* ln(concentration), Fig. 5a—were measured and the critical aggregation concentration (*cac*) determined as usual at the inflection point of the curve. A noteworthy feature is that for $x_{CTAB} > 0.67$, there is a minimum in surface tension at about *cac* (highest for 0.90), which seems to indicate that on increasing the bulk concentration above *cac* the composition at the interface changes, and so the surface tension changes before attaining a stable value. This type of behavior has been reported for other catanionic mixtures.[64] An explanation for it could be that as the mixed micelles form in the bulk they start depleting the surface from CTAB, which is more surface-active than SOSo, until equilibrium is reached. From Fig. 5b, *cac* values in the x_{CTAB} = 0.90–0.10 range decrease significantly compared to x_{CTAB} = 1 (neat CTAB, *cmc* = 0.9 mmol kg^{-1}) and 0 (neat SOSo, *cmc* = 150 mmol kg^{-1}), clustering at around 0.20–0.25 mmol kg^{-1}. Similarly, the surface tension values at *cac*, γ_{cac}, lie at *ca.* 30 mN m^{-1}, lower than those for neat CTAB (34 mN m^{-1}) and SOSo (42 mN m^{-1}).

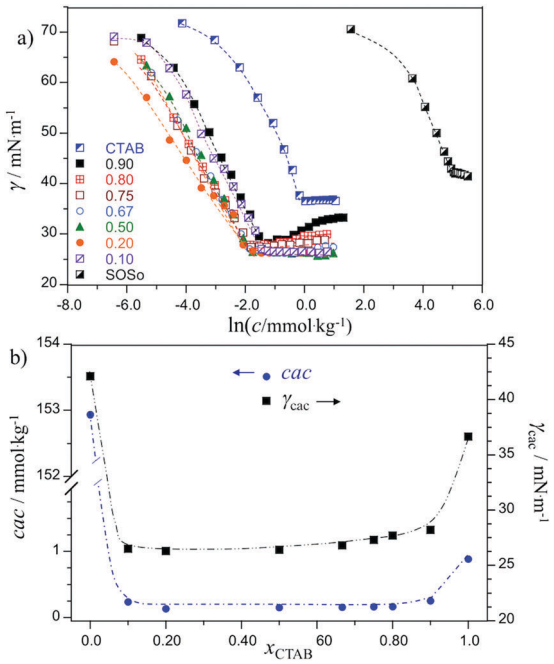

Fig. 5 Surface tension data at 27.0 °C: (a) γ *vs.* logarithm of total surfactant concentration; (b) *cac* and γ_{cac} as a function of x_{CTAB} (lines are visual guides).

The *cac* values allow calculating the β parameter,[47,65,66] a dimensionless value used to evaluate the degree of synergism (within the regular solution approximation) and defined as:

$$\beta = z\frac{\Delta w}{k_B T} \quad (2)$$

where $\Delta w = w_{12} - \frac{1}{2}(w_{11} + w_{22})$ and w_{ij} is the pairwise interaction energies between molecules i and j, z is the number of nearest neighbors, k_B is the Boltzmann constant and T is the absolute temperature (for calculation of β from the data see ESI,† Section 3).

Large negative values of β indicate strong attractive interactions and hence negative deviations from ideal mixing behavior. β values in the CTAB/SOSo yield an average $\beta = -16 \pm 1$, in line with similar systems.[3,67,68] Altogether, the results demonstrate that there is indeed a strong attractive interaction between the two molecules.

3.4. Micelles and vesicles inside the foam

Knowledge of the bulk self-assembly structure is not sufficient to predict foam stability. Preliminary results in Section 3.1 show that foam is very unstable in the anionic-rich side, $x_{CTAB} < 0.50$, while samples can be foamed in the cationic-rich one. However, polydisperse vesicles are found in samples from x_{CTAB} = 0.10–0.51, so samples with vesicles can have very different abilities to stabilize foam. SOSo is a highly soluble molecule, and on its own incapable of stabilizing foam even at high concentrations. This is because of the very high solubility of the short chain surfactant, resulting in fast exchange at the interface, and incapacity to sustain surface tension gradients to have sufficient surface elasticity to stabilize foam films.[39,69] Indeed, stable foams or foam films cannot be made with many surfactant types with 8 or 10 carbons in the tail (depending on headgroup type).[37,70] Therefore, as soon as there is too much SOSo, the foams are unstable probably due to the very low elasticity that SOSo confers to the surfaces, which means that they are no longer stable against coalescence. Similarly in foams made from 1 : 1 mixtures of weakly interacting surfactants (β-$C_{12}G_2$ and $C_{12}E_6$), the foam stability was found determined by the less stable species ($C_{12}E_6$).[40]

Although the bulk self-assembly is not sufficient to predict foam stability, it is not clear whether the assembly inside a foam is the same as in bulk. Several things can perturb bulk assembly: (i) during generation of foam the solutions experience high shear rates; (ii) foams are characterized by high surface-to-volume ratios, which can change the surfactant distribution; and (iii) films thinner than the characteristic size of vesicles or elongated micelles are found. In order to verify if any of these factors influence the assembly of our mixtures in foams, SANS experiments on foams were carried out.

For the SANS studies we have chosen 3 samples forming vesicles, rodlike micelles and small micelles, so x_{CTAB} = 0.50, 0.60 and 0.80, respectively, all at 20 mmol kg^{-1}. The foams studied were made with air saturated with C_6F_{14} to ensure that their evolution was slow on the time-scale of the SANS measurements (60 min at longest) and the liquid fraction is 20%. The samples were made in a solvent of D_2O to ensure good contrast between the surfactants and the solvent and the air–water interfaces and the solvent.[71] The scattered intensities for the corresponding bulk samples and foams are shown in Fig. 6.

At the lowest q, the scattering from the foams in Fig. 6 has a q^{-4} contribution arising from the air–water interfaces.[71] This is typical of Porod scattering and can be described using:

$$I(q) = 2\pi(\Delta SLD)^2 \frac{S}{V} q^{-4} \quad (3)$$

The intensity depends on ΔSLD, the difference in scattering length densities of air and D_2O (6.39×10^{-6} Å^{-2}) and the specific surface S/V (amount of gas/water surface per unit volume), with $S = N4\pi R^2$ and $V = N(4\pi R^3)/\{3(1 - \varphi)\}$ which gives $S/V = 3(1 - \varphi)/R$. Here N is the number of bubbles, R is the average bubble radius and φ the liquid fraction in the foam.

Therefore, we can fit the data to obtain the average radius of the bubbles. The black lines in Fig. 6 are fits to the data, and the resulting average bubble radii are 78, 45 and 35 μm for the 0.80, 0.60 and 0.50 samples, respectively. These values are in good agreement with measurements under the microscope in the first minutes after foam generation, where 29, 17 and 20 μm were measured for the three samples (x_{CTAB} = 0.80, 0.60 and 0.50). The bubbles with x_{CTAB} = 0.80 are larger than with the other two samples. The values obtained from SANS are slightly bigger probably because the radii are not measured in the first minutes, but typically up to one hour after generation (the measurements take *ca.* 60 min and they start at most 3 min after the generation of foam).

The intensities scattered by the foams are also lower than the bulk solutions at medium to high q. The number of micelles or vesicles is smaller than in the bulk samples because 80% of the

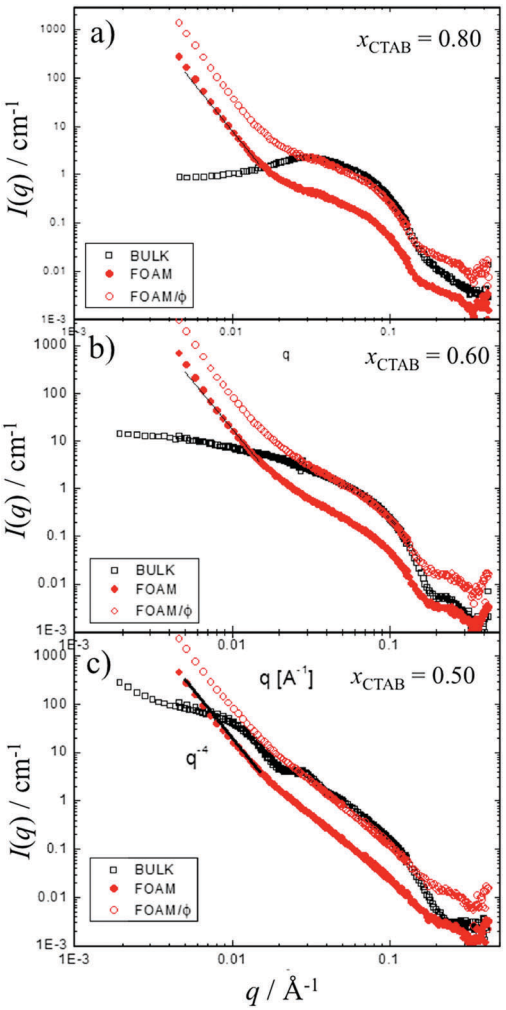

Fig. 6 SANS spectra of bulk solutions (black squares), of foams generated at ϕ = 20% (filled red circles) and the same foams divided by ϕ (empty red circles) for samples: 0.80 (a), 0.60 (b), and 0.50 (c). The black line is a fit to the data using eqn (3).

volume is air. If we plot $I(q)/\phi$, the intensities become comparable for all the samples. This means that the liquid fraction has not changed significantly after generation and remains at 20%. We can also compare the scattering patterns, which are very alike at x_{CTAB} = 0.60 and 0.80 allowing to conclude that the elliptical and rodlike micelles are the same in and out of foams. The scattering from the foam with x_{CTAB} = 0.50 is very featureless, but this is because the oscillations linked to the vesicle sizes are at lower q-values where the q^{-4} from the bubble surfaces dominates. Therefore, even at x_{CTAB} = 0.50 little difference in the self-assembly structure is expected. Foams have been studied at liquid fractions of 10, 15, 20 and 25% (see Fig. S4, ESI†) and in all of them consistent self-assembly structures were found between bulk and foam. Having established that the self-assembly structure has not changed during the passage from bulk to foam, we can analyze the foam stability in terms of the bulk properties.

Different 20 mmol kg^{-1} x_{CTAB} solutions are foamed at ϕ = 20% and stored inside glass vials in order to evaluate foam stability. The bubbles are made with air containing traces of

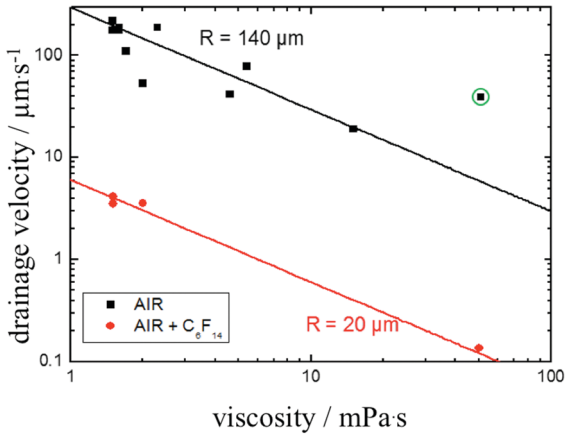

Fig. 7 Drainage velocity as a function of viscosity for foams generated at 20% ϕ with air (in black) or with traces of fluorinated gas (in red). The lines are estimated drainage velocities using eqn (4) with R = 140 μm for the foams with air and in H_2O (black line) and R = 20 μm for the foams with C_6F_{14} and in D_2O (red line).

C_6F_{14}, like in the SANS experiments or simply with air. The foams made with no traces of C_6F_{14} coarsen much faster than those with the fluorinated gas. One way to evaluate foam stability is to measure the foam drainage velocity. The drainage velocity is measured from the amount of liquid that drains out of the foam. The drainage velocities of the different samples are plotted in Fig. 7 as a function of bulk viscosity, with the viscosity taken at the estimated shear rate during drainage.

The foam drainage velocity, v, can be estimated assuming immobile interfaces (no slip boundary condition) in the steady state with no capillary effects and constant liquid fraction within the foam as:[72]

$$v = K_C \rho g L^2 \varphi / \mu \quad (4)$$

with K_C a dimensionless number linked to foam permeability, which from simulations is shown to be 1/150 for immobile interfaces, ρg the gravitational stress, L the length of a Plateau border, which we can estimate as 0.72R, φ the liquid fraction and μ the viscosity. The size of the bubbles has a strong influence on the drainage velocity, as together with the liquid fraction it sets the size of the channels. The bubble size for the foams with traces of C_6F_{14} evolves slowly and R = 20 μm is used to adjust the data, as shown by the red line in Fig. 7. In the foams prepared with air, the bubble size evolves quickly in the first minutes and we use the radius as a fit parameter, where R = 140 μm is found to describe the data well (black line in Fig. 7); it is a reasonable estimate considering visual observations of the bubbles during aging. The fits describe the drainage well, suggesting that independent of the self-assembly structures the foam drainage is well described using the drainage equation developed for simple fluids, as has been previously found for the drainage of foams with polymer solutions.[73] We note however, the order of magnitude difference between the expected drainage velocity and the measured drainage velocity for the sample with x_{CTAB} = 0.60 made with air (circled in green). The foam drains much faster than it could be expected

to, and this could suggest that the elongated micelles are capable of aligning in the Plateau borders. This is not at all the case for the samples made with traces of C_6F_{14}, possibly because the drainage velocity is so much slower that it is incapable of aligning the micelles.

The bubble size was measured after one week in foams made with traces of C_6F_{14}. The sizes for x_{CTAB} = 0.80, 0.60 and 0.50 were 650, 450 and 330 μm respectively. Very little coalescence is observed in these samples; therefore it can be assumed that the bubble size increases only because of coarsening. If the film permeabilities were the same for all the samples, one would expect to finish with similar sized bubbles for x_{CTAB} = 0.80 and 0.50 as the drainage velocities are similar, and the 0.60 could be smaller as the drainage is much slower (with C_6F_{14} not with air only).[74] Coarsening of a wetter foam is slower than a drier foam.[26] However, we find that the smallest bubbles are those with x_{CTAB} = 0.50. This suggests that the permeability of the interfaces is smaller for this mixture, with the most equal mixing of CTAB and SOSo of the foaming samples.

3.5. Overview

We have studied solutions and foams made from mixtures of CTAB and SOSo. Due to the opposite charges of the molecules, they readily associate together and variation of the molar ratio leads to a variety of assembly structures and to changes in foam stability. CTAB has a low *cmc* (0.91 mmol kg^{-1}), forms small elliptical micelles and is also an effective foam stabilizer. SOSo is very soluble (*cmc* = 153 mmol kg^{-1}) and incapable of stabilizing any foam. Adding SOSo to CTAB leads initially ($x_{CTAB} \geq 0.80$) to very slight changes in the micellar form and foam stability from that of neat CTAB. Increase of SOSo concentration (decrease of x_{CTAB}) results in changes in the composition of the micelles, as more of the SOSo is in the assemblies. The electrostatic repulsion between the headgroups is decreased, counterions are released and the micelles become elongated. The elongated micelles have a high viscosity, which makes the solutions more difficult to foam, but the resulting foams are more stable against drainage, as the flow slowed down. As equimolar mixtures are approached ($x_{CTAB} \approx 0.50$) vesicles are formed; however, these vesicles are positively charged indicating that considerable SOSo remains in solution in unimeric form. Once $x_{CTAB} < 0.50$, vesicles are formed and they phase-separate around 0.30 as the assemblies likely become equimolar and zero-charged. However, in this SOSo-rich region there are no foams: SOSo-laden surfaces cannot sustain sufficient surface tension gradients in these conditions, and the bubbles coalesce very quickly and foams disappear before they are fully formed.

4. Conclusion

To summarize, we have shown that the studied self-assembled structures are not modified by the foaming process or foam properties, but the foam stability can be rationalized in terms of the bulk solution properties. Bulk and foams in the CTAB/SOSo catanionic system contain the same type of aggregates at similar x_{CTAB} as revealed by SANS, which allows us to use results of bulk characterization to discuss foam stability. Significantly, the self-assembly and foam production and stability depend critically on x_{CTAB}. CTAB-rich compositions containing small ellipsoidal micelles and vesicles foam well, but are relatively unstable, whereas foams in the rodlike micelle region are more difficult to generate but are considerably more stable due to the solution viscosity. On the other hand, the SOSo-rich samples, which contain vesicles, foam poorly and foams collapse quickly, because the SOSo-laden surfaces cannot sustain sufficient surface tension gradients to stabilize foam films in these conditions, which is a first requirement in stable foam design. From this work we could then extract a more general conclusion that self-assembly structure is not the appropriate parameter to predict foam stability. However, once the bubbles can be formed and a foam stabilized, the bulk-assembly and surfactant synergism can control the time-scales of drainage and coarsening, hence aiding the stabilization of the foams.

Conflicts of interest

There are no conflicts to declare.

Acknowledgements

We are grateful to Dominique Langevin for useful discussions. For the cryo-TEM experiments, the authors acknowledge financial support from the French CNRS (FR3507), the CEA METSA network (www.metsa.fr), and the "Investissements d'Avenir" of the LabEx PALM (ANR-10-LABX-0039-PALM). Sambath Saranga and Vincent Klein are also gratefully acknowledged for technical help with the foam experiments. We also acknowledge financial support from the Science and Technology Foundation (FCT), Portugal, and FEDER/COMPETE through grants UID/QUI/00081/2013, POCI-01-0145-FEDER-006980 and NORTE-01-0145-FEDER-000028.

References

1 B. Kronberg, K. Holmberg and B. Lindman, *Surface Chemistry of Surfactants and Polymers*, John Wiley & Sons, Chichester, 2014.
2 Q. Zhou and M. J. Rosen, *Langmuir*, 2003, **19**, 4555–4562.
3 A. Khan and E. F. Marques, *Curr. Opin. Colloid Interface Sci.*, 1999, **4**, 402–410.
4 S. Bardhan, K. Kundu, B. Kar, G. Chakraborty, D. Ghosh, D. Sarkar, S. Das, S. Senapati, S. K. Saha and B. K. Paul, *RSC Adv.*, 2016, **6**, 55104–55116.
5 J. C. Fountain, A. Klimek, M. G. Beikirch and T. M. Middleton, *J. Hazard. Mater.*, 1991, **28**, 295–311.
6 S. Mahiuddin, O. Zech, S. Raith, D. Touraud and W. Kunz, *Langmuir*, 2009, **25**, 12516–12521.

7 T. Kijima, T. Yoshimura, M. Uota, T. Ikeda, D. Fujikawa, S. Mouri and S. Uoyama, *Angew. Chem., Int. Ed.*, 2004, **43**, 228–232.

8 S. M. Dong, P. T. Spicer, F. P. Lucien and P. B. Zetterlund, *Soft Matter*, 2015, **11**, 8613–8620.

9 K. Margulis-Goshen, B. F. B. Silva, E. F. Marques and S. Magdassi, *Soft Matter*, 2011, **7**, 9359–9365.

10 V. Croce, T. Cosgrove, C. A. Dreiss, G. Maitland, T. Hughes and G. Karlsson, *Langmuir*, 2004, **20**, 7984–7990.

11 P. Koshy, V. K. Aswal, M. Venkatesh and P. A. Hassan, *Soft Matter*, 2011, **7**, 4778–4786.

12 Y. Lin, X. Han, J. Huang, H. Fu and C. Yu, *J. Colloid Interface Sci.*, 2009, **330**, 449–455.

13 H. L. Wu, C. Ramachandran, N. D. Weiner and B. J. Roessler, *Int. J. Pharm.*, 2001, **220**, 63–75.

14 T. Bramer, N. Dew and K. Edsman, *J. Pharm. Pharmacol.*, 2007, **59**, 1319–1334.

15 J. Bhattacharjee, G. Verma, V. K. Aswal, A. A. Date, M. S. Nagarsenker and P. A. Hassan, *J. Phys. Chem. B*, 2010, **114**, 16414–16421.

16 R. Zhang and P. Somasundaran, *Adv. Colloid Interface Sci.*, 2006, **123**, 213–229.

17 L. R. Arriaga, D. Varade, D. Carriere, W. Drenckhan and D. Langevin, *Langmuir*, 2013, **29**, 3214–3222.

18 D. Varade, D. Carriere, L. R. Arriaga, A. L. Fameau, E. Rio, D. Langevin and W. Drenckhan, *Soft Matter*, 2011, **7**, 6557–6570.

19 A. Stocco, D. Carriere, M. Cottat and D. Langevin, *Langmuir*, 2010, **26**, 10663–10669.

20 H. Fauser, M. Uhlig, R. Miller and R. von Klitzing, *J. Phys. Chem. B*, 2015, **119**, 12877–12886.

21 Z. Xue, A. J. Worthen, C. Da, A. Qajar, I. R. Ketchum, S. Alzobaidi, C. Huh, M. Prodanovic and K. P. Johnston, *Langmuir*, 2016, **32**, 28–37.

22 E. Rio, W. Drenckhan, A. Salonen and D. Langevin, *Adv. Colloid Interface Sci.*, 2014, **205**, 74–86.

23 D. Langevin, *Adv. Colloid Interface Sci.*, 2000, **88**, 209–222.

24 A.-L. Fameau and A. Salonen, *C. R. Phys.*, 2014, **15**, 748–760.

25 A.-L. Fameau, A. Saint-Jalmes, F. Cousin, B. Houinsou Houssou, B. Novales, L. Navailles, F. Nallet, C. Gaillard, F. Boué and J.-P. Douliez, *Angew. Chem., Int. Ed.*, 2011, **50**, 8264–8269.

26 I. Cantat, S. Cohen-Addad, F. Elias, F. Graner, R. Höhler, O. Pitois, F. Rouyer and A. Saint-Jalmes, *Foams Structure and Dynamics*, Oxford University Press, Oxford, 2013.

27 P. Stevenson, *Foam Engineering: Fundamentals and Applications*, John Wiley & Sons, Chichester, 2012.

28 K. Małysa, *Adv. Colloid Interface Sci.*, 1992, **40**, 37–83.

29 D. Weaire, S. Hutzler, G. Verbist and E. Peters, *Advances in Chemical Physics*, John Wiley & Sons, Inc., 2007, pp. 315–374, ch 5, DOI: 10.1002/9780470141618.

30 D. Langevin and E. Rio, *Encyclopedia of Surface and Colloid Science*, Taylor and Francis, New York, 2012, pp. 1–15.

31 M. Safouane, M. Durand, A. Saint Jalmes, D. Langevin and V. Bergeron, *J. Phys. IV*, 2001, **11**, Pr6-275–Pr276-280.

32 E. Rio and A. L. Biance, *ChemPhysChem*, 2014, **15**, 3692–3707.

33 Z. Briceño-Ahumada, A. Soltero, A. Maldonado, J. Perez, D. Langevin and M. Impéror-Clerc, *Colloids Surf., A*, 2016, **507**, 110–117.

34 R. M. Guillermic, A. Salonen, J. Emile and A. Saint-Jalmes, *Soft Matter*, 2009, **5**, 4975–4982.

35 J. Goyon, F. Bertrand, O. Pitois and G. Ovarlez, *Phys. Rev. Lett.*, 2010, **104**, 128301.

36 A. Salonen, R. Lhermerout, E. Rio, D. Langevin and A. Saint-Jalmes, *Soft Matter*, 2012, **8**, 699–706.

37 C. Stubenrauch and K. Khristov, *J. Colloid Interface Sci.*, 2005, **286**, 710–718.

38 V. Bergeron, *Langmuir*, 1997, **13**, 3474–3482.

39 P. R. Garrett and P. R. Moore, *J. Colloid Interface Sci.*, 1993, **159**, 214–225.

40 C. Stubenrauch, L. K. Shrestha, D. Varade, I. Johansson, G. Olanya, K. Aramaki and P. Claesson, *Soft Matter*, 2009, **5**, 3070–3080.

41 A. Salonen, M. In, J. Emile and A. Saint-Jalmes, *Soft Matter*, 2010, **6**, 2271–2281.

42 E. F. Marques, R. O. Brito, S. G. Silva, J. E. Rodríguez-Borges, M. L. D. Vale, P. Gomes, M. J. Araújo and O. Söderman, *Langmuir*, 2008, **24**, 11009–11017.

43 L. L. Brasher and E. W. Kaler, *Langmuir*, 1996, **12**, 6270–6276.

44 B. F. B. Silva, E. F. Marques and U. Olsson, *Soft Matter*, 2011, **7**, 225–236.

45 C. Zhou, X. Cheng, O. Zhao, S. Liu, C. Liu, J. Wang and J. Huang, *Soft Matter*, 2014, **10**, 8023–8030.

46 Y. J. Wang and E. F. Marques, *J. Phys. Chem. B*, 2006, **110**, 1151–1157.

47 R. M. F. Fernandes, E. F. Marques, B. F. B. Silva and Y. Wang, *J. Mol. Liq.*, 2010, **157**, 113–118.

48 N. Schelero, A. Stocco, H. Möhwald and T. Zemb, *Soft Matter*, 2011, **7**, 10694–10700.

49 N. Schelero, H. Lichtenfeld, H. Zastrow, H. Möhwald, M. Dubois and T. Zemb, *Colloids Surf., A*, 2009, **337**, 146–153.

50 L. L. Brasher, K. L. Herrington and E. W. Kaler, *Langmuir*, 1995, **11**, 4267–4277.

51 H. T. Jung, S. Y. Lee, E. W. Kaler, B. Coldren and J. A. Zasadzinski, *Proc. Natl. Acad. Sci. U. S. A.*, 2002, **99**, 15318–15322.

52 S. G. Silva, M. L. C. do Vale and E. F. Marques, *Chem. – Eur. J.*, 2015, **21**, 4092–4101.

53 J. C. Hao and H. Hoffmann, *Curr. Opin. Colloid Interface Sci.*, 2004, **9**, 279–293.

54 B. F. B. Silva, E. F. Marques and U. Olsson, *J. Phys. Chem. B*, 2007, **111**, 13520–13526.

55 B. F. B. Silva, E. F. Marques and U. Olsson, *Langmuir*, 2008, **24**, 10746–10754.

56 A. Brulet, D. Lairez, A. Lapp and J. P. Cotton, *J. Appl. Crystallogr.*, 2007, **40**, 165–177.

57 T. Gaillard, M. Roché, C. Honorez, M. Jumeau, A. Balan, C. Jedrzejczyk and W. Drenckhan, *Int. J. Multiphase Flow*, 2017, **96**, 173–187.

58 K. K. Karukstis, S. A. McCormack, T. M. McQueen and K. F. Goto, *Langmuir*, 2004, **20**, 64–72.

59 S. Zhang and H. N. Teng, *Colloid J.*, 2008, **70**, 105–111.

60 K. L. Herrington, E. W. Kaler, D. D. Miller, J. A. Zasadzinski and S. Chiruvolu, *J. Phys. Chem.*, 1993, **97**, 13792–13802.
61 E. Cappelaere and R. Cressely, *Colloid Polym. Sci.*, 1998, **276**, 1050–1056.
62 S. Ozeki and S. Ikeda, *J. Colloid Interface Sci.*, 1980, **77**, 219–231.
63 F. Kern, R. Zana and S. J. Candau, *Langmuir*, 1991, **7**, 1344–1351.
64 C. Liu, J. Hao and Z. Wu, *J. Phys. Chem. B*, 2010, **114**, 9795–9804.
65 A. A. McLachlan and D. G. Marangoni, *J. Colloid Interface Sci.*, 2006, **295**, 243–248.
66 Y. Wang and E. F. Marques, *J. Mol. Liq.*, 2008, **142**, 136–142.
67 C. Pucci, L. Perez, C. La Mesa and R. Pons, *Soft Matter*, 2014, **10**, 9657–9667.
68 S. B. Lioi, X. Wang, M. R. Islam, E. J. Danoff and D. S. English, *Phys. Chem. Chem. Phys.*, 2009, **11**, 9315–9325.
69 R. Tuinier, C. G. J. Bisperink, C. van den Berg and A. Prins, *J. Colloid Interface Sci.*, 1996, **179**, 327–334.
70 J. Schlarmann and C. Stubenrauch, *Tenside, Surfactants, Deterg.*, 2003, **40**, 190–195.
71 A. Mikhailovskaya, L. Zhang, F. Cousin, F. Boué, P. Yazhgur, F. Muller, C. Gay and A. Salonen, *Adv. Colloid Interface Sci.*, 2017, DOI: 10.1016/j.cis.2017.07.024.
72 A. Saint-Jalmes, *Soft Matter*, 2006, **2**, 836–849.
73 M. Safouane, A. Saint-Jalmes, V. Bergeron and D. Langevin, *Eur. Phys. J. E: Soft Matter Biol. Phys.*, 2006, **19**, 195–202.
74 Z. Briceno-Ahumada and D. Langevin, *Adv. Colloid Interface Sci.*, 2017, **244**, 124–131.